Materials Characterization 194 (2022) 112454

Contents lists available at ScienceDirect

Materials Characterization

journal homepage: www.elsevier.com/locate/matchar

Laser powder bed fusion of high-strength and corrosion-resistant Inconel alloy 725

C.J. Todaro [a,b], M. Rashidi [a], R.L. Liu [a,c], S. Gao [a], T.P. Le [a], J.E. Fronda [a], J. Setyadji [a], Y.T. Tang [d], M. Seita [a,e,*]

[a] School of Mechanical and Aerospace Engineering, Nanyang Technological University, Singapore
[b] Department of Mechanical Engineering, University College London, WC1E 7JE, UK
[c] Singapore Centre for Environmental Life Sciences Engineering, Nanyang Technological University, Singapore
[d] Department of Materials, University of Oxford, Parks Road, Oxford OX1 3PH, UK
[e] Department of Engineering, University of Cambridge, Trumpington Street, Cambridge CB2 1PZ, UK

ARTICLE INFO

Keywords:
Additive manufacturing
3D printing
Powder bed fusion
Superalloy
Inconel 725
Microstructure
Tensile properties
Corrosion properties

ABSTRACT

The development of additive manufacturing, or three-dimensional (3D) printing, technologies has produced breakthroughs in the design and manufacturing of products by enhancing design freedom and minimising manufacturing steps. In addition, the complex, unique microstructures imparted by the additive processes offer prospects of unprecedented advances to produce high-performance metal alloys for high-temperature and corrosive environments. Here, we present the first additive manufacturing of Inconel alloy 725, an advanced nickel-base superalloy that is the widely accepted gold standard material of choice for oil and gas, chemical, and marine applications. We explore the printability of Inconel alloy 725 and identify a wide processing space to build material with a crack- and near-pore-free microstructure. The conventionally heat-treated Inconel alloy 725 has an equiaxed, near-fully recrystallised microstructure containing copious twin boundaries and nano-precipitates. It also displays promising tensile properties and corrosion resistance compared to its wrought counterpart. Our work opens the door toward additive manufacturing of Inconel alloy 725 components with optimised microstructure and topology geometry for applications in harsh environments.

1. Introduction

Additive manufacturing (AM), or three-dimensional (3D) printing, has revolutionised manufacturing across all major industrial sectors, including aeronautics, automotive, biomedical, construction, space, and many others [1–4]. In contrast to traditional subtractive manufacturing, which produces parts by removing material, AM builds parts by successively adding material in a layer-wise fashion. This process results in reduced material waste, minimised manufacturing steps, and enhanced design freedom. AM is deemed a disruptive technology for making metal alloy components for load-bearing applications [5]. The additive process offers added design freedom that can directly impact the performance and lifetime of parts made from structural metal alloys. For example, superalloy turbine blades with complex internal cooling channels can be produced by AM [6], eliminating the need for expensive ceramic investment moulds as required by traditional manufacturing routes. In another instance of added design freedom, AM is capable of fabricating parts with 3D architected lattices or truss networks with effective material use and optimised strength-to-weight ratios [7].

Besides geometry-related improvements in part performance, AM can impart unique microstructures that enhance the failure resistance of metallic materials. One example is AM of austenitic stainless steels, which can show an exceptional combination of high tensile properties [8], corrosion resistance [9], and hydrogen embrittlement resistance [10]. The performance improvements stem from the additional strengthening mechanisms brought about by the formation of solidification cellular structures [8,11], suppression of second-phase precipitates [9], and phase stability of the material during deformation [10], which are ascribed to the non-equilibrium cooling conditions of the AM process. Furthermore, AM enables structural materials with unprecedented property tuning through composition [12] or microstructure adjustments [13,14]. These adjustments can be tailored locally by varying the process parameters or feedstock material point-by-point in the printed part. As an example, one could make components by AM

* Corresponding author at: School of Mechanical and Aerospace Engineering, Nanyang Technological University, Singapore.
E-mail address: ms2932@cam.ac.uk (M. Seita).

https://doi.org/10.1016/j.matchar.2022.112454
Received 10 August 2022; Received in revised form 11 October 2022; Accepted 31 October 2022
Available online 4 November 2022

that are tough and ductile on the inside while resistant to failure or degradation on the outside skin, by, for instance, locally manipulating the composition [15], grain size and morphology [16], grain boundary network [17], or phase distribution [18].

This new materials design paradigm could easily find an application in the oil and gas, chemical, and marine industries, which have a history of catastrophic failures. Unlike other sectors like automotive and aerospace, these industries have been slow to adopt AM since most of the potential printed parts are critical components that must withstand extreme conditions. In the years ahead, AM is poised to broadly reshape industries like oil and gas where parts can be stored digitally and manufactured on-demand in offshore facilities, removing costly logistics and warehousing. Designing new metal alloys from scratch for AM, while certainly needed, can be prohibitively time-consuming and costly. Adapting current grades of metal alloys to AM can be more cost-effective with shorter design cycles. One promising commercial alloy to engineer by AM is Inconel alloy 725 (IN725, UNS N07725), an age-hardening nickel-chromium-molybdenum-niobium-based superalloy that combines the excellent strength and toughness found in Inconel alloy 718 (IN718) with the corrosion resistance displayed by Inconel alloy 625 (IN625) [19]. A notable example of catastrophic mechanical failure of the IN725 includes the recent field failure of a part made from wrought material [20]. The failure is believed to be associated with stress corrosion- and/or hydrogen-induced cracking. AM may provide a practical solution to these problems by leveraging its enhanced part and microstructure design freedom. Although many studies report on the printability of commercial nickel-base superalloys (see Table 1), AM of IN725 has yet to be explored.

Here, we report on the AM of IN725 by laser-based powder bed fusion (L-PBF) for the first time. We assess the printability of IN725 using a Prager-Shira diagram and thermodynamic modelling, and predict that the material is resistant to cracking during L-PBF. We explore the scan speed-hatch distance space for L-PBF IN725 and identify a wide region to build material with a crack- and near-pore-free (relative density of >99.5%) microstructure. We characterise the grain structure of near-defect-free IN725 before and after heat treatment, consistent with ASTM standards. Strongly textured, coarse columnar grains appear in the as-printed metal alloy. By contrast, upon heat treatment, the metal alloy shows a near-fully recrystallised microstructure with fine, equiaxed recrystallised grains containing copious twin boundaries and nano-precipitates. The tensile properties of the L-PBF IN725 in the heat-treated condition meet the strength-ductility requirement for its wrought counterpart. The AM metal alloy also shows promising corrosion resistance compared to conventional wrought material. Our work opens a pathway toward AM IN725 components that can provide extended service under extremely harsh environments.

Table 1
Summary of commercial nickel-base superalloys built by AM.

Alloy	Institute	Year	Ref.
Inconel alloy 718	Northwestern Polytechnical University, China	2008	[21]
Inconel alloy 625	University of Michigan, USA	2009	[22]
Inconel alloy 738LC	ETH Zurich, Switzerland	2013	[23]
Inconel alloy 939	University of Paderborn, Germany	2013	[24]
CM247LC	University of Birmingham, UK	2014	[25]
Inconel alloy 100	Singapore Institute of Manufacturing Technology, Singapore	2014	[26]
CMSX-4	Georgia Institute of Technology, USA	2014	[27]
Inconel alloy 792	Institute of Metal Research, China	2018	[28]
Haynes 282	Wayne State University, USA	2019	[29]
Inconel alloy 713C	University of Sheffield, UK	2020	[30]
Inconel alloy 725	Nanyang Technological University, Singapore	2022	This work

2. Methods

2.1. Thermodynamic modelling

We calculated the solidification path of IN725 using Thermo-Calc Software (www.thermocalc.com) [31] with a Scheil-Gulliver solidification model and TTNi8 thermodynamic database. We obtained the solidification path of IN725 under the same conditions with the same procedure as for other commercial nickel-base superalloys [32]. We assessed the printability of IN725 by comparing the risk to strain-age cracking and hot tearing between IN725 and other commercial nickel-base superalloys (data previously reported in ref. [32]). We defined the freezing range (ΔT_f) of alloys as the temperature range between the liquidus temperature ($T_{fs=0}$) and the temperature corresponding to a solid fraction of 0.99 ($T_{fs=0.99}$).

2.2. Sample preparation

We produced samples of IN725 from gas-atomised powder (25–63 μm in diameter, supplied by Carpenter Technology Corporation, Fig. 1a) with a nominal composition shown in Table 2. We built the samples using a custom-made L-PBF printer equipped with a pulsed fibre laser (SPI Lasers, G4) with a central emission wavelength of 1060 nm and maximum average power of 200 W. We produced two sets of samples with rectangular and dog-bone shapes, respectively (Fig. 1b). The first was 3 mm in width, 7.5 mm in height, and 15 mm in length. The second had a gauge length of 10 mm, gauge width of 2 mm, and height of 15 mm. To build the block samples, we set the laser power (P) to 200 W, beam diameter (D) to 110 μm, and layer thickness (t) to 50 μm. We varied the scan speed (v) between 400 and 900 mm s^{-1} and the hatch spacing (h) between 45 and 120 μm. We chose to fix the laser power to the printer's maximum value (200 W) since the process window for producing defect-free L-PBF metal alloys widens with increasing laser power, as shown in previous work [33]. We then chose to vary scan speed and hatch distance, both of which contribute to pore formation in L-PBF [34,35]. To build the dog-bone-shaped sample, we set $P = 200$ W, $t = 50$ μm, $D = 110$ μm, $v = 700$ mm s^{-1}, and $h = 60$ μm. In this work, these specific parameters led to builds with the highest density. During the L-PBF of both sample sets, we chose a raster scan pattern with an increment of 67° between each layer and used nitrogen as the shielding gas. No preheating was used during the L-PBF process.

We cut the block samples along the *y-z* cross-section and prepared their surfaces by standard metallurgical procedures. We selected the block sample produced with optimised process parameters (i.e., those used to build the dog-bone-shaped samples) for detailed microstructural characterisation in both the as-printed and heat-treated conditions. We followed a heat-treatment regime (Fig. 1c) consisting of a solution treatment (1040 °C for 1 h followed by water quenching) followed by ageing (732 °C for 8 h followed by furnace cooling to 621 °C, holding 8 h, and air cooling), as per the 2017 ASTM B805 standard (*Standard Specification for Precipitation Hardening Nickel Alloys Bar and Wire* [36]).

2.3. Microstructural characterisation

We measured the areal porosity of each block sample using images of their entire cross-sections obtained with an optical microscope. We examined the grain structure of the as-printed and heat-treated L-PBF IN725 by electron backscatter diffraction (EBSD) in a scanning electron microscope (JEOL, JSM-7800F PRIME) equipped with an EBSD detector (Oxford Instruments, Symmetry S2). We carried out EBSD using a step size of 500 nm, accelerating voltage of 20 kV, and working distance of 20 mm. We analysed the EBSD data using the software AztecCrystal (www.nano.oxinst.com). We identified the phases in the gas-atomised powder as well as in the L-PBF IN725, both in the as-printed and heat-

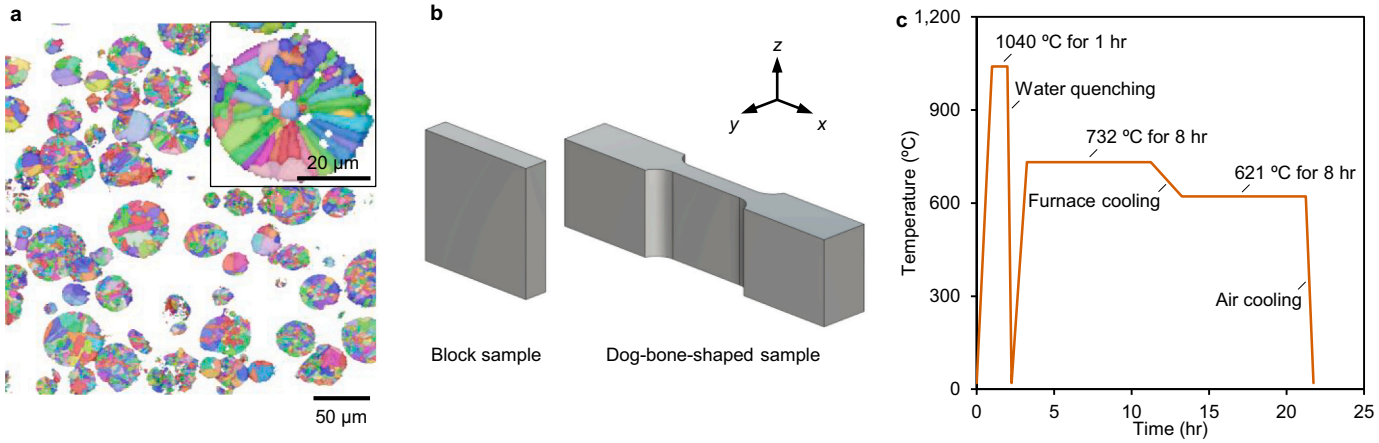

Fig. 1. L-PBF and heat treatment of IN725. a Inverse pole figure map along the out-of-plane direction of gas-atomised IN725 powder. Inset, small circular regions of un-indexed pixels inside of an IN725 polished powder, presumably representing porosity. b Schematic of the block and dog-bone-shaped samples with their *z*-axis parallel to the build direction. c Schematic overview of the heat treatment regime applied herein.

Table 2
RMIT Classification: Trusted

Alloy	Cr	Mo	Fe	Nb	Ti	Al	B	Co	Ta	Si	Mn	C	Mg	Cu	O	N	Ni
IN725	19.43	7.40	4.44	3.78	1.71	0.66	0.004	0.01	0.065	0.01	0.01	0.013	0.01	0.05	0.006	0.004	Bal.

treated conditions, using an X-ray diffractometer (Malvern Panalytical, Empyrean) with Cu $K\alpha_1$ radiation. We inspected the distribution and morphology of precipitates in the as-printed and heat-treated L-PBF IN725 using transmission electron microscopy (TEM, JEOL, JEM-2100F). We prepare the TEM lamellae using a focused ion beam (FIB) microscope (ZEISS, Crossbeam 540).

2.4. Tensile testing

We prepared tensile specimens with a thickness of 1 mm by sectioning the dog-bone-shaped sample with electrical discharge machining. We polished both sides of the gauge section by standard metallurgical procedures. We performed tensile testing at an initial strain rate of 1×10^{-3} s^{-1}, using a universal testing machine (Shimadzu, AGS-50kNX) equipped with a non-contact digital video extensometer (Shimadzu, TRViewX). We compared the values of strength and ductility obtained from tensile testing (averaged over three repeats for both the as-printed and heat-treated L-PBF IN725) with the tensile requirements for wrought IN725, as per the 2017 ASTM B805 standard [36].

2.5. Electrochemical and corrosion testing

We performed potentiodynamic polarisation testing to assess the corrosion behaviour of PBF IN725, both in the as-printed and heat-treated conditions. We compared the results to those obtained from wrought IN725. The wrought IN725 exhibits a fully recrystallised, precipitation-hardened microstructure, as studied previously [37,38]. We used a BioLogic potentiostat controlled by the software EC-Lab (BioLogic). We mounted the specimens in epoxy resin with one side exposed to the electrolyte and the opposite side electrically connected to the working electrode via a copper wire. We ground and polished the exposed side of the samples to a #2000 grit finish and then ultrasonically cleaned them with ethanol. We perform the potentiodynamic polarisation in a conventional flat cell comprising a working electrode (the tested specimen with the exposed surface area of ~0.5 cm^2), silver-silver chloride reference electrode, and platinum mesh counter electrode (~2 cm^2). We selected 3.5 wt% NaCl solution as the electrolyte, and we conditioned the specimens in electrolyte for 1 h to stabilise an open circuit potential before the testing. We carried out polarisation scans in a linear upward manner from −0.25 V (vs. open circuit potential) to 1 $V_{Ag/AgCl}$ with a scanning rate of 1 mV s^{-1} and limiting current density of 1 mA cm^{-2} in a naturally aerated condition at room temperature (25 °C). We repeated the tests at least three times per sample to ensure good reproducibility.

3. Results

3.1. Alloy manufacturability via L-PBF

The high-temperature strength of nickel-base superalloys derives from the fine-scale precipitates of the γ' ($L1_2$, primitive cubic) and γ" ($D0_{22}$, body-centred tetragonal) phases in the ductile γ matrix (A1, face-centred-cubic, FCC) [39]. Many nickel-base superalloys are unsuitable for fusion-based AM due to their rapid precipitation of γ' and/or γ" particles following solidification, which hinders the relaxation of stresses in the age-hardened material, resulting in strain-age cracking [40]. The susceptibility of nickel-base superalloys to strain-age cracking is often explained using Prager-Shira diagrams [41], which show that increasing the content of γ'- and γ"-forming elements (e.g., aluminium, titanium, niobium, tantalum, etc.) increases the propensity of nickel-base superalloys to strain-age cracking. Originally developed for welding technologies [41], these diagrams have been adapted for evaluating the risk of nickel-base superalloys to strain-age cracking during fusion-based AM [32]. In Fig. 2a, we plot a modified Prager-Shira diagram for various commercial nickel-base superalloys. Following an empirical rule, an alloy tends to strain-age cracking if the weight percentages of aluminium, titanium, niobium, and tantalum are $W_{Al} + 0.5W_{Ti} + 0.3W_{Nb} + 0.15W_{Ta} > 4$ wt%. The diagram indicates that IN725 is the least susceptible of the precipitation-hardening alloys studied to strain-age cracking.

Another possible issue with the manufacturability of IN725 by L-PBF is cracking during solidification, often termed hot tearing or solidification cracking [42]. The Scheil-Gulliver model for solidification and freezing range are often used to predict the susceptibility of an alloy to hot tearing. A large freezing range ΔT_f usually leads to less liquid being available for feeding along grain boundaries near the end of

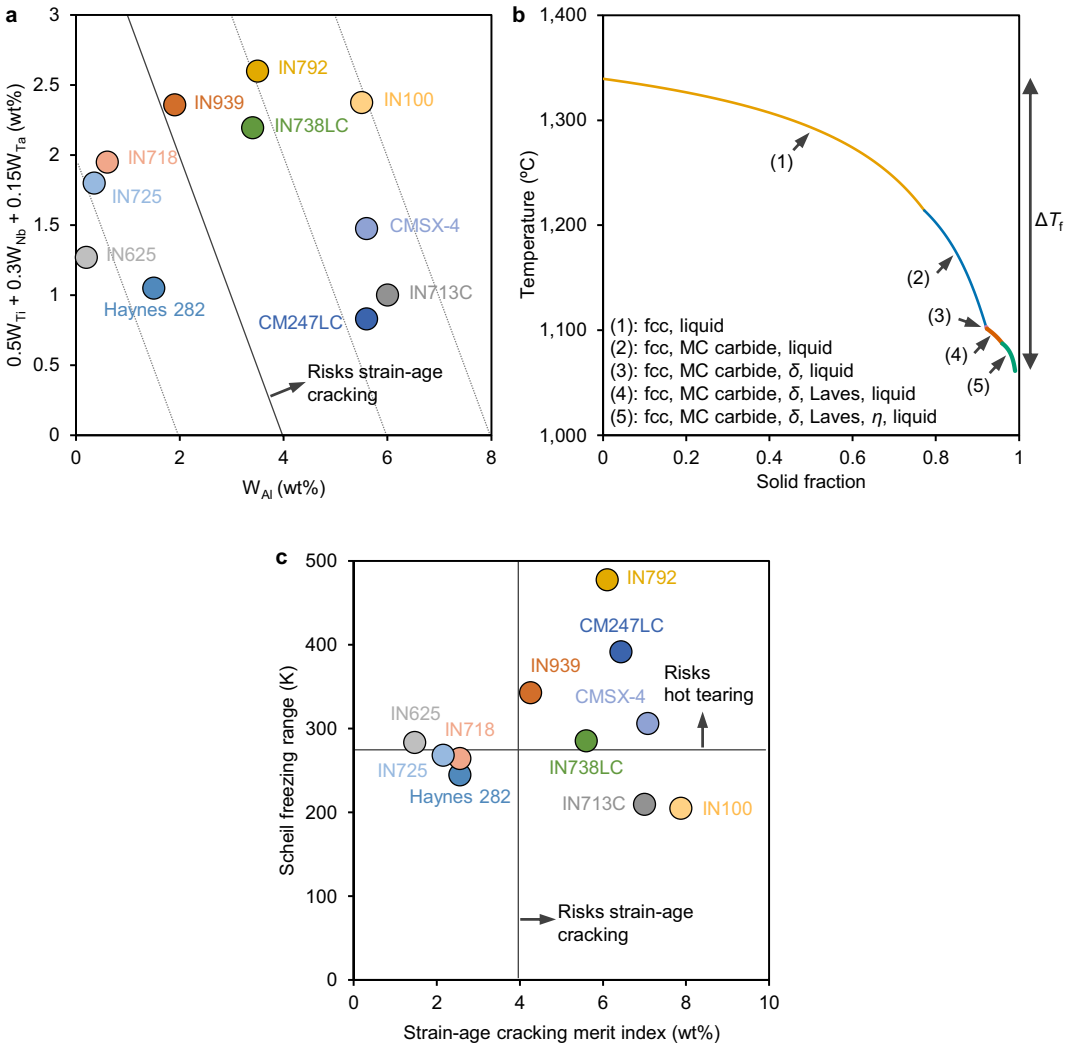

Fig. 2. Risk of cracking of IN725 during fusion-based AM. a A modified Prager-Shira diagram for various commercial nickel-base superalloys. b The Scheil-Gulliver solidification path of IN725. c The freezing range ΔT_f of various commercial nickel-base superalloys versus their strain-age cracking merit index M_{SAC}.

solidification to resist cracking. Based on our thermodynamic predictions using the Scheil-Gulliver model, the freezing range ΔT_f of IN725 is 268 K (Fig. 2b). To evaluate the likelihood of IN725 to hot tearing, we plot the freezing range ΔT_f of various commercial nickel-base superalloys versus their strain-age cracking merit index [32] ($M_{SAC} = W_{Al} + 0.5W_{Ti} + 0.3W_{Nb} + 0.15W_{Ta}$) (Fig. 3c). The freezing range ΔT_f limit for risk to hot tearing of 280 K is, to a first approximation as has been assumed previously [32], between that of Inconel alloy 738LC (285 K) and IN718 (265 K). The former often suffers from hot tearing [43,44], while the latter frequently resists it [45,46]. Based on this plot, our thermodynamic modelling predicts that IN725 resists hot tearing during fusion-based AM.

A closer examination of the solidification path of IN725 (Fig. 2b) suggests that there is no rapid drop in temperature in the last stages of solidification, which is crucial for the printability of superalloys [32]. A solidification cracking index (SCI) developed by Kou [47] can be used to further assess the susceptibility of an alloy to cracking during solidification by determining the maximum steepness of its curve of temperature (T) versus the square root of fraction solid ($f_s^{1/2}$):

$$\mathrm{SCI} = \left| dT/d\left(f_s^{1/2}\right) \right| \quad (1)$$

We calculate the SCI for IN725 over the last stages of solidification (f_s = 0.9–0.99) to be 2021 K. The SCI value of IN725 is comparable to other printable alloys such as IN718 (921 K) and ABD-850 AM (3577 K) and much lower than those of difficult-to-process alloys such as Inconel 939 (7170 K) and Inconel 738LC (6681 K) [32]. This SCI analysis helps to further rationalise the low solidification crack susceptibility of IN725 during fusion-based AM.

3.2. Processing parameter space

To identify v-h combinations (i.e., scan speed-hatch distance) for defect-free L-PBF IN725, we quantify the porosity in an array of 36 samples with different v (400, 500, 600, 700, 800 and 900 mm s^{-1}) and h (45, 60, 75, 90, 105 and 120 μm) values by optical microscopy. In Fig. 3a, we plot the porosity of each sample (proportional to the bubble size) versus v (x-axis) and volumetric energy density (E, y-axis). The latter represents the energy transferred to the powder bed for melting and is typically expressed as $E = \frac{P}{vht}$. We identify three key regions in this processing parameter space for L-PBF IN725: (1) risk of keyhole defects for $v \leq 600$ mm s^{-1}, (2) risk of lack-of-fusion defects for $v \geq 700$ mm s^{-1} and $E \leq 74$ J mm^{-3}; and (3) near-porosity-free builds for $v \geq 700$ mm s^{-1} and $E > 74$ J mm^{-3}. Fig. 3b-d show some representative optical micrographs of these three cases. We find that the near-porosity-free builds have E values of 74–127 J mm^{-3}. This finding is in good agreement with what has been reported in the literature for L-PBF IN625 (60–100 J mm^{-3}) [48] and L-PBF IN718 (80–110 J mm^{-3}) [49]. Low scan speeds v

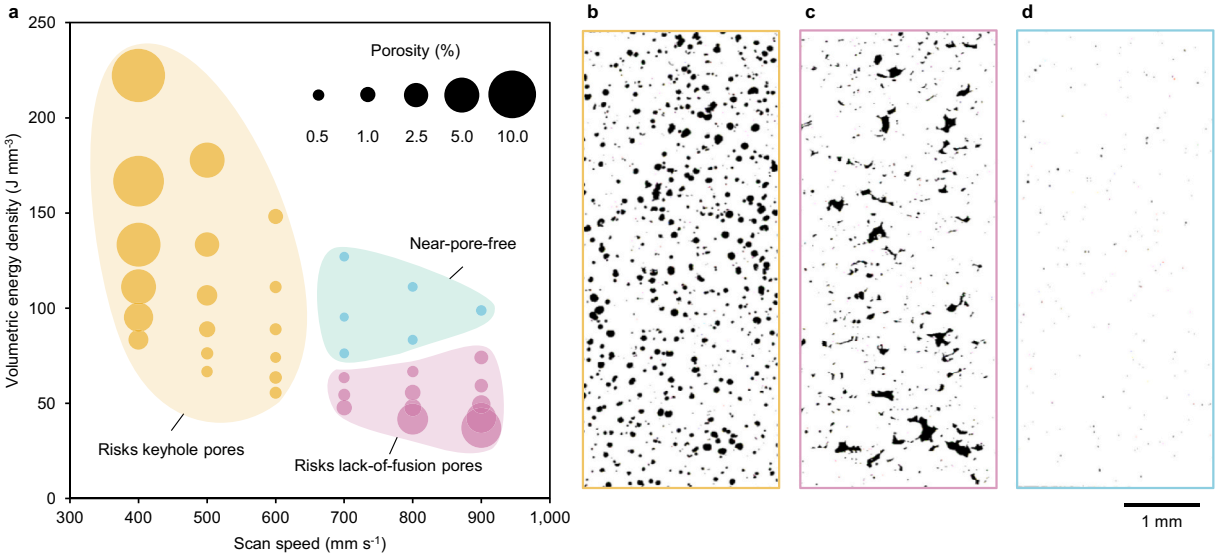

Fig. 3. L-PBF of near-defect-free IN725. a A bubble plot showing porosity in samples as a function of scan speed v (x-axis) and volumetric energy density E (y-axis). b-d Optical images showing representative samples with keyhole pores ($E = 222$ J mm^{-3} and $v = 400$ mm s^{-1}) (b), lack-of-fusion pores ($E = 37$ J mm^{-3} and $v = 900$ mm s^{-1}) (c) and near-defect free microstructure ($E = 95$ J mm^{-3} and $v = 700$ mm s^{-1}) (d).

are known to result in spherical keyhole pores, which are associated with local recoil pressure on the liquid below the laser due to intense vaporisation [35]. On the other hand, combinations of high scan speeds v and low volumetric energy densities E can result in lack-of-fusion pores, which originate from inadequate fusion bonding among successive hatches and layers [34]. We observe no cracks in any of the samples consistent with the predictions of our qualitative analysis (Fig. 2). We highlight that, under optimal conditions, porosity in L-PBF IN718 and L-PBF IN625 can be reduced to around 0.1–0.2%, which is lower than what we have achieved in this work. We expect that the increased residual porosity in this work stems from porosity in our gas-atomised powder, which was produced in a small batch. Indeed, we observe small circular regions of un-indexed pixels inside some powder particles (Fig. 1a).

Throughout the rest of the paper, we focus on samples produced using $v = 700$ mm s^{-1} and $h = 60$ μm, which yield the densest builds (relative density of ~99.6%).

3.3. Grain structure

To analyse the grain structure of our samples, we plot EBSD inverse pole figure grain maps of the as-printed and heat-treated metal alloy (Fig. 4). The as-printed metal alloy shows a series of large columnar grains (several hundred micrometres in length) aligned along the build direction, z, and having a strong $\langle 100 \rangle_z$ fibre texture (maximum value of multiples of uniform density of 7.1) (Fig. 4a). Comparable textures have been obtained for other nickel-based metal alloys printed using the same raster scan strategy employed in this work [50,51]. The EBSD measurements further indicate that the as-printed metal alloy contains a large fraction of low-angle grain boundaries (49% of the total grain boundaries) (Fig. 4b). We compute the average grain size based on the high-angle grain boundaries in Fig. 4b to be 173 μm. The grain orientation spread map in Fig. 4c shows that the misorientation between each measured point in a grain and the average orientation of the grain is substantial, and amounts to an average of 5.9° (Fig. 4c). Large intragranular orientation spread often implies the presence of geometric necessary dislocation (GND) structures within grains, which are another common feature of as-printed metal alloys produced by L-PBF. We determine the average GND density in as-printed L-PBF IN725 using the orientation data collected by EBSD and the Weighted Burgers Vector technique to be 0.39×10^{14} m^{-2}. Such microstructural features are hypothesised to originate from the compression-tension stresses rendered by the localised heating and cooling cycles upon laser scanning [52].

In comparison, the heat-treated alloy shows mostly randomly oriented equiaxed grains containing many $\Sigma 3\{111\}$ <110> coherent twin boundaries (CTBs) and average grain size of 68 μm (computed by including all CTBs) (Fig. 4d). The heat treatment has not only replaced many of the low-angle grain boundaries with $\Sigma 3$ CTBs (56% of the total grain boundaries) but also markedly reduced the average spread in orientation within grains from 5.9° to 1.1° (as evidenced when comparing Fig. 4b to e and c to f). The heat treatment has also reduced the average GND density to 0.14×10^{14} m^{-2}, about a third of that estimated before heat treatment. These features are indicative of recrystallisation. Intragranular orientation spread is often used as a means to distinguish recrystallised from non-recrystallised grains, where the orientation spread within the former is lower than that of the latter [53]. We select values of grain orientation spread smaller than 2° to isolate recrystallised grains and compute their occurrence in both the as-printed and heat-treated microstructures. We find an increase in the area percentage of recrystallised grains from 28% to 89% upon heat treatment. We conclude that our L-PBF IN725 undergoes rapid recrystallisation upon heat treatment (within the short treatment time of 1 h) and without any additional thermomechanical processing. This is in contrast to the recrystallisation of L-PBF 316 L, which requires additional mechanical deformation before heat treatment at 1050 °C [54].

To assess the solidification structure of L-PBF IN725 and its evolution upon heat treatment, we use a combination of backscattered electron (BSE) imaging and EBSD (Fig. 5a-d). The BSE micrograph of the as-printed metal alloy (Fig. 5a) shows solidification cells about a micron wide within the grains of high orientation spread (Fig. 5b). Conversely, the heat-treated microstructure exhibits no cells within recrystallised grains (Fig. 5c, d). Hence, we conclude that recrystallisation during heat treatment eliminates the cell structure. We note that the polished surfaces of both the as-printed and heat-treated IN725 do not show any obvious second-phase particles within grains or at grain boundaries by SEM, suggesting that no second-phase particles are distinguishable at the micrometre scale. After etching their polished surfaces, we find thin films at intercellular regions of the as-printed IN725 (Supplementary Fig. 1). We expect that the films are either solute-enriched FCC γ matrix or secondary phases (e.g., Laves), forming by solute segregation during solidification. To further identify the phases in our samples, we analyse

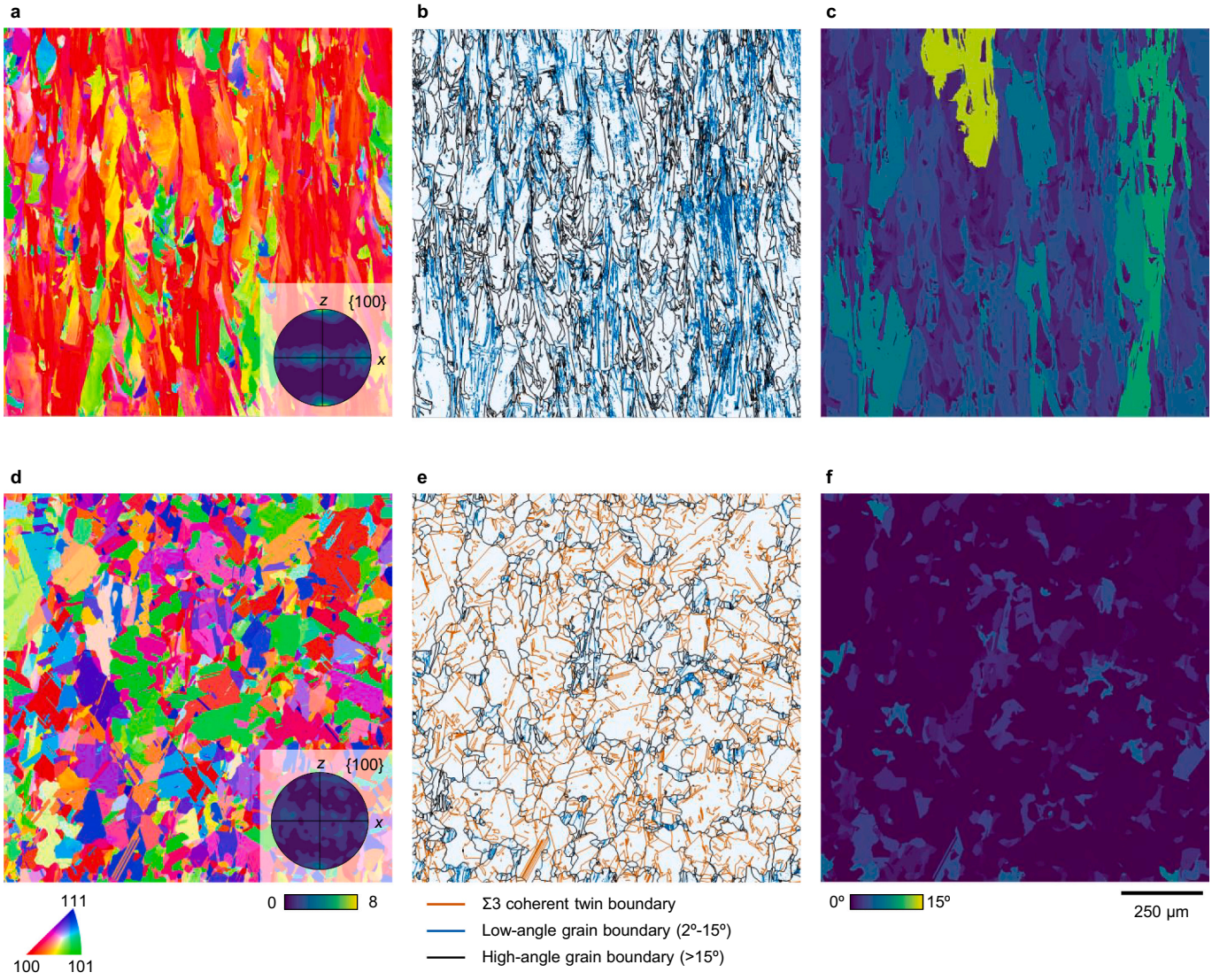

Fig. 4. Grain structure of L-PBF IN725. EBSD analysis of the as-printed (a-c) and heat-treated (d-f) alloy. a, d EBSD inverse pole figure maps along the *z*-axis. Insets show the corresponding {100} contoured pole figures. b, e Grain boundary maps. c, f Grain misorientation maps.

the x-ray diffraction (XRD) measurements of the as-printed and heat-treated metal alloy, as well as the pre-alloyed powder, which we take as reference (Fig. 5e). The X-ray diffraction patterns confirm the possibility of the FCC γ matrix, γ'-, and/or γ"-precipitates in the L-PBF IN725. We cannot resolve these phases because their peaks overlap with each other. We resolve such phases by TEM in the next section.

3.4. Precipitation of intermetallic phases

We rely on TEM to investigate the presence of precipitates in our samples. The results, shown in Fig. 6, indicate the absence of precipitates inside the as-printed metal alloy but their presence in the heat-treated one. Selected area diffraction of the as-printed alloy reveals electron diffraction spots of single-phase FCC γ matrix (Fig. 6a). Selected-area electron diffraction of the heat-treated metal alloy shows additional superlattice diffraction spots corresponding to other phases (Fig. 6b). We adopt the $[001]_{\gamma}$ zone axis to unambiguously identify the precipitates, following the technique of Paulonis et al. [55] and the theoretical diffraction patterns given in Ref. [56]. In this orientation, the diffraction pattern shows electron diffraction spots belonging to γ'- and γ"-precipitates. Thus, the (001) spot marked by the arrow in Fig. 6b is composed of a point, which is a $(001)_{\gamma'}$ reflection, and a streak, which is a $(002)_{\gamma''}$ reflection. We capture the detailed geometry and distribution of γ"-precipitates, which are the principle strengthening particles in γ"-precipitate-containing nickel-base superalloys [39]. Fig. 6c shows the dark-field TEM image of γ"-precipitates taken from the $(101)_{\gamma''}$ reflection marked by the orange circle. The precipitates are uniformly distributed within the FCC γ matrix and have disk-shaped geometry, with a length of ~9 nm and width of ~3 nm. These results are comparable to what has been reported for wrought IN725 [37]. We do not observe any other obvious secondary phases in our TEM specimens. Nonetheless, we cannot ignore the possibility that second-phase particles (e.g., Laves, carbides, oxides, δ, etc.) exist in our alloy, which demands in-depth TEM experiments to verify [57].

3.5. Tensile properties

To assess the mechanical properties of L-PBF IN725, we plot the engineering stress-strain behaviour of the alloy in tension—both in the as-printed and heat-treated conditions—and compare the results against the 2017 ASTM B805 standard for wrought IN725 [36], as well as the literature data on L-PBF IN625 [58] and L-PBF IN718 [59] which were heat-treated following ASTM standards. We show the experimental results in Fig. 7a and detail the tensile properties in Table 3. Comparing

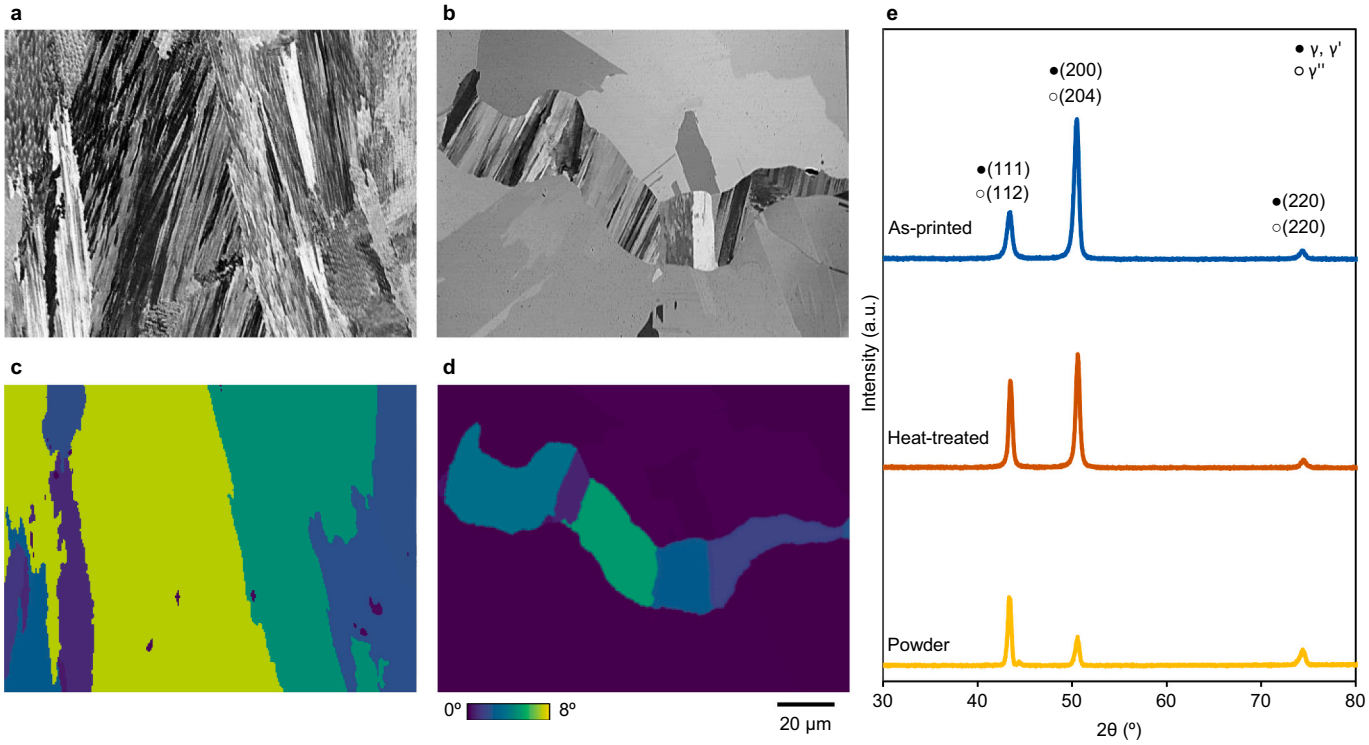

Fig. 5. Solidification structure and phases in L-PBF IN725. a, b BSE images acquired by SEM of the as-printed (a) and heat-treated (b) alloy. c, d Grain misorientation maps acquired by EBSD of the as-printed (c) and heat-treated (d) metal alloy from the same regions shown in a and b, respectively. e XRD patterns of our L-PBF samples and the gas-atomised powder.

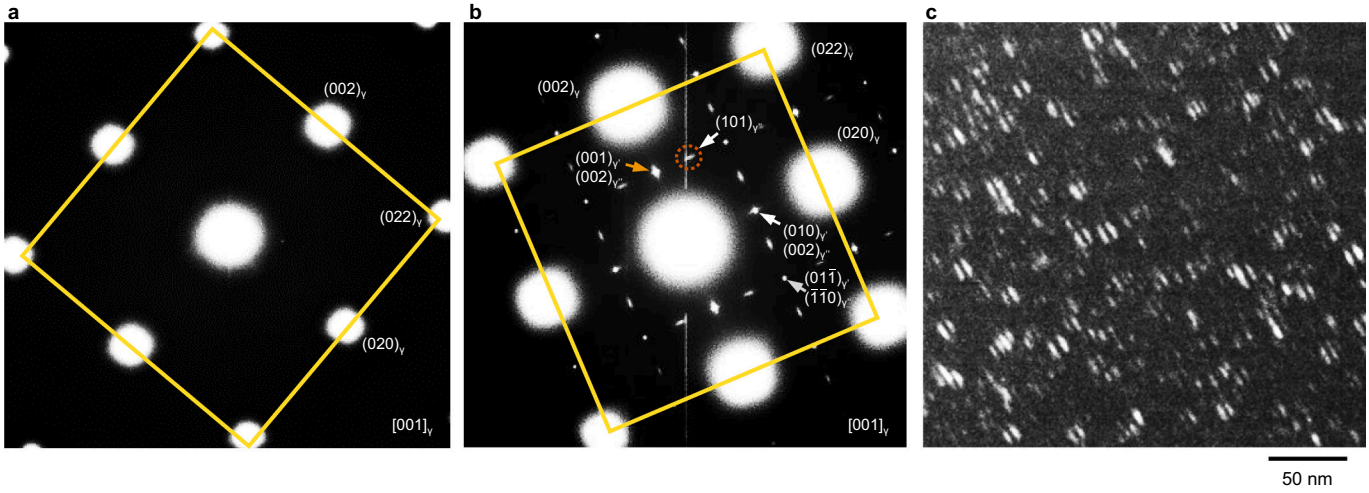

Fig. 6. Precipitates in L-PBF IN725. a, b Selected-area electron diffraction patterns with the $[001]_\gamma$ zone axis for the as-printed (a) and heat-treated (b) metal alloy. c Dark-field TEM image taken from the (101) reflection marked by the red circle in b, highlighting coherently diffracting domains corresponding to γ''-precipitates. (For interpretation of the references to colour in this figure legend, the reader is referred to the web version of this article.)

the as-printed and heat-treated alloy, we note an increase in the strength of the metal alloy after heat treatment (~42% and ~26% increase in yield strength, σ_y, and ultimate tensile strength, σ_{UTS}, respectively) but a decrease in elongation at fracture (ε_f, ~23% decrease). The fracture surfaces of both samples mostly consist of ~700 nm-sized dimples (Fig. 7a, b), which is indicative of void coalescence during ductile fracture. The heat-treated L-PBF IN725 meets the requirements of tensile properties for conventional wrought material. When comparing the different L-PBF metal alloys in their standard heat-treated conditions, IN725 exhibits strengths and an elongation till fracture in between those of IN625 and IN718.

3.6. Corrosion properties

To characterise the corrosion behaviour of our samples, we perform potentiodynamic polarisation tests on the as-printed and heat-treated L-PBF IN725 and compare the results against the wrought counterpart. Fig. 8 displays the typical polarisation curves for each material in 3.5 wt % NaCl. Such gcurves are widely used to benchmark the corrosion resistance of metallic materials in different environments [60]. Following repeated tests, we detail the average characteristic corrosion values for our samples in Table 4. The polarisation curves of both the L-PBF IN725 and wrought IN725 specimens display a similar polarisation

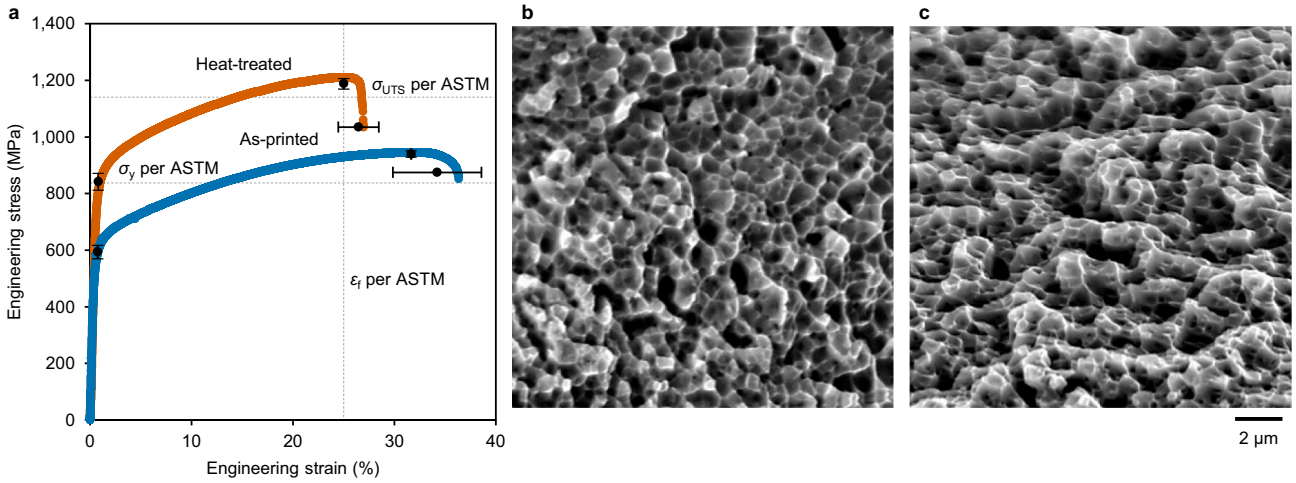

Fig. 7. Tensile testing of L-PBF IN725. a Representative engineering stress-strain curves of the as-printed and heat-treated metal alloy; error bars represent one standard deviation. b, c SEM micrographs of the fracture surfaces of the as-printed (b) and heat-treated (c) metal alloy.

Table 3
Mechanical properties of selected nickel-base superalloys.

Alloy	Condition	Yield strength, σ_y (MPa)	Ultimate tensile strength, σ_{UTS} (MPa)	Elongation at fracture, ε_f (%)	Ref.
L-PBF IN725	As-printed	593	940	34.2	This work
	Heat-treated	842	1188	26.5	
Wrought IN725	Heat-treated	827	1137	25	[36]
L-PBF IN625	Heat-treated	650	917	47	[58]
L-PBF IN718	Heat-treated	1102	1362	10.1	[59]

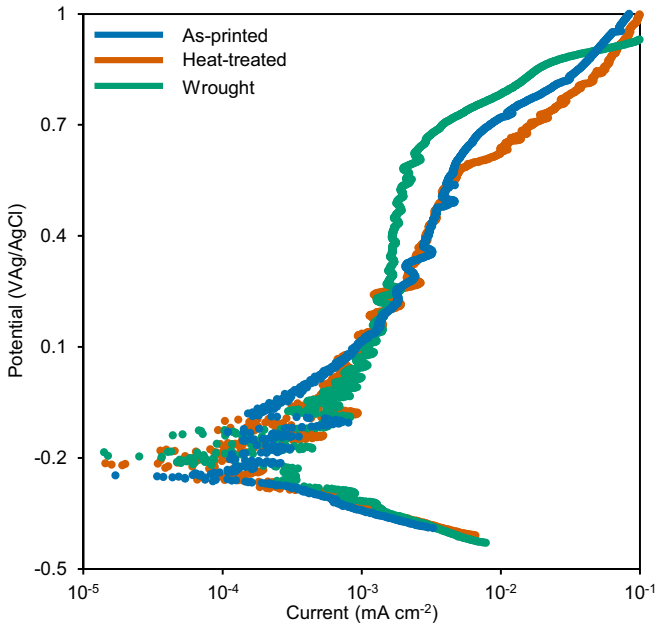

Fig. 8. Potentiodynamic polarisation curves for L-PBF IN725 in the as-printed and heat-treated conditions in 3.5 wt% NaCl. Results for the wrought counterpart are included for comparison.

Table 4
Characteristic corrosion values of IN725 determined from potentiodynamic polarisation in 3.5 wt% NaCl. Results for L-PBF IN718 under similar conditions from the literature are included for comparison.

Alloy	Condition	Corrosion potential, E_{corr} ($V_{Ag/AgCl}$)	Corrosion current, i_{corr} (μA cm^{-2})	Pitting potential, E_{pit}, ($V_{Ag/AgCl}$)
L-PBF IN725	As-printed	−0.23 ± 0.02	2.66 ± 0.21	0.61 ± 0.01
L-PBF IN725	Heat-treated	−0.21 ± 0.01	2.33 ± 0.40	0.59 ± 0.02
Wrought IN725	Heat-treated	−0.20 ± 0.02	3.24 ± 0.42	0.65 ± 0.01

response in the active region of the anodic branch (approximately below 120 mV anodic overpotential). We note corrosion potential E_{corr} values for the L-PBF and wrought specimens in the range of −0.21 to −0.23 $V_{Ag/AgCl}$, slightly more negative than that of the wrought metal alloy (−0.2 $V_{Ag/AgCl}$). We also note that the extrapolated values of I_{corr} for the metal alloys tested herein are similar, where the difference in I_{corr} between the L-PBF and wrought samples is <1 μA cm^{-2}. These results signal that our L-PBF IN725—both in the as-printed and heat-treated conditions—exhibits a comparable nobility and corrosion rate to its wrought counterpart. Interestingly, upon transition to the passive region, we measure a relatively lower anodic Tafel-slope and higher passive current density in the passive potential range of ~0.25 to 0.5 $V_{Ag/AgCl}$ for the L-PBF specimens compared to the wrought specimens. This observation is in good agreement with the less noble E_{pit} values measured for the as-printed (0.61 $V_{Ag/AgCl}$) and heat-treated (0.59 $V_{Ag/AgCl}$) specimens as opposed to the wrought ones (0.65 $V_{Ag/AgCl}$). The minor effect of heat treatment on the corrosion values of L-PBF IN725 is consistent with what has been reported for L-PBF IN718 following a similar heat treatment regime [61].(

4. Discussion

In this work, we have shown that IN725 can be included in the palette of metallic materials which can be readily manufactured by L-PBF. More specifically, we carried out the first analyses of the risk of IN725 to cracking during fusion-based AM using a Prager-Shira diagram and thermodynamic modelling. Such a methodology has been proven effective for evaluating the printability of metal alloys in fusion-based AM [32]. Our assessment revealed a tendency of IN725 to resist cracking during fusion-based AM, with comparable behaviour to that of

the well-studied, easily printable metal alloys IN718 and IN625. Our experimental results validated the high resistance of IN725 to cracking during L-PBF, in which we obtained crack-free samples across the entire processing window studied herein. We also identified a wide processing window for printing IN725 with near-porosity-free (relative density of >99.5%) microstructures. Our work demonstrates excellent printability of L-PBF IN725, that is, the ability of the metal alloy to print with a crack- and near pore-free microstructure by L-PBF. The wide processing window suggests the possibility of further engineering the microstructure of the metal alloy during printing by tuning processing parameters, to optimise combinations of mechanical and corrosion properties.

The as-printed L-PBF IN725 displayed textured columnar grains and fine solidification cell structures. Such a microstructure is well reported in many commercial metal alloys produced by L-PBF, including similar metal alloys IN625 [58] and IN718 [62], and is attributed to the intrinsic high cooling rates and high temperature gradients of the manufacturing process [63,64]. By contrast, the heat-treated L-PBF IN725 showed mostly randomly oriented recrystallised equiaxed grains having a high density of Σ3 CTBs and no evidence of solidification cells. Previous work on L-PBF austenitic stainless steel revealed that, during heat treatment, Σ3 CTBs nucleate new recrystallised grains with mobile grain boundaries that sweep and consume the as-printed microstructure [65]. The high fraction of Σ3 CTBs in the heat-treated L-PBF IN725 likely aided the massive recrystallisation of the metal alloy during heat treatment.

The recrystallisation response of the L-PBF IN725 to standard heat treatment is unlike other commercial L-PBF nickel-base superalloys. For instance, standardised heat treatments (following both wrought [66] and AM [67] standards) do not trigger recrystallisation of L-PBF IN718, which instead requires substantially higher solution treatment temperatures of >1100 °C [62,68–70]. Similar observations were made in studies on L-PBF IN625 [71], where solution treatments using temperatures of only the utmost limit (>1080 °C) given by the standard [72] result in recrystallization. Recrystallisation can aid the release of age-hardening constituents (niobium, titanium and aluminium) into the nickel matrix by dissolving second-phase particles [73] and cell networks. Also, recrystallisation often results replaces columnar grains with equiaxed ones. Equiaxed grains are conducive to isotropic mechanical properties and therefore more desirable for structural applications, in general. Previous work found that as-printed IN718 exhibits higher strength but lower ductility in the *x*-direction compared to the *z*-direction due to columnar grains aligned along the build direction [74]. Thus, we expect that the tensile data reported herein for the as-printed IN725 represent upper and lower bounds for the strengths and elongation, respectively. In addition, previous research demonstrated that a L-PBF IN718 with a heat treatment-inducing recrystallised microstructure possesses near-isotropic tensile properties along different loading directions [75]. In this regard, although the tensile data are limited to one direction herein, we expect that our heat-treated L-PBF IN725 with recrystallised grain structure should exhibit near-isotropic tensile properties. Our work shows that the recrystallisation temperature of L-PBF IN725 is satisfied by standard heat treatment. In this regard, L-PBF IN725 together with the standard heat treatment are uniquely well-suited for attaining a well-homogenised and near-fully recrystallised grain structure.

The heat-treated L-PBF IN725 exhibits strength and ductility that meet the requirements of the ASTM standard for conventional wrought material. The yield strength σ_y of the L-PBF IN725 increased by ~42% after heat treatment. The as-printed and heat-treated microstructures showed a large difference in GND and cellular structures (both substantial in the as-printed sample but sparse in the heat-treated one) and CTBs and strengthening-precipitates (only present in the heat-treated sample). The presence of each of these microstructural features can enhance the strength of metal alloys by blocking dislocation movement. Our results, therefore, suggest that the primary contributing factor to the strengthening of L-PBF IN725 are the nano-precipitates and CTBs while the secondary contributing factors are the GND and cellular structures.

The mechanical performance of our L-PBF IN725, which is lower than that of IN718 but higher than IN625, can be rationalized based on the classic strength-ductility trade-off, where most metallurgical mechanisms for increasing strength lead to a loss in ductility. Based on their composition of γ''-forming elements, IN718 exhibits increased precipitation-hardening over IN725, while IN625 possesses limited precipitation-hardening and is often considered non-precipitation-hardenable. Hence, the variation in mechanical properties between the different metal alloys may be explained by their precipitation-hardenability, per the strength-ductility paradigm. We importantly note that many studies have shown that newly designed heat treatments that shift away from industry standards can provide optimised mechanical performance combinations in L-PBF IN718 [57,76] and L-PBF IN625 [71,77,78]. This points to opportunities to enhance the mechanical properties of our L-PBF IN725 by tailoring the heat treatment, and we believe this is an important area for future work.

The heat-treated L-PBF IN725 showed corrosion characteristics comparable to that of wrought metal alloy, owing to their analogous microstructure, i.e., essentially fully recrystallised grains containing a high density of nano-precipitates. Despite being free of precipitates—which can increase susceptibility to corrosion by promoting strong micro-galvanic corrosion [79]—the as-printed L-PBF IN725 exhibits similar corrosion behaviour to the two precipitate-containing samples (heat-treated wrought and L-PBF IN725). Other microstructural features such as residual stresses and cellular structures, including accompanying GND networks and LAGBs, may increase the propensity of as-printed AM metal alloys to corrosion [80]. Future dedicated experiments are required to elucidate the individual contributions of such microstructural features to the corrosion behaviour of as-printed AM metal alloys.

5. Conclusion

We have additively manufactured Inconel alloy 725 (IN725), for the first time, by laser-based powder bed fusion (L-PBF). Our conclusions are as follows:

- We assessed the printability of IN725 using a Prager-Shira diagram and thermodynamic modelling. Our assessment predicted the metal alloy resists cracking during AM.
- We explored the processing space for L-PBF IN725 and identified a wide region to print the material with a crack- and near-pore-free (relative density of >99.5%) microstructure. The wide processing region suggests the possibility of further engineering the microstructure and performance of the metal alloy during AM by tuning processing parameters.
- We characterised the grain structure of near-defect-free IN725 before and after conventional heat treatment. Strongly textured, coarse columnar grains appear in the as-printed metal alloy. By contrast, upon heat treatment, the metal alloy shows a near-fully recrystallised microstructure with fine, equiaxed grains containing many twin boundaries and strengthening precipitates.
- We assessed the tensile and corrosion performance of L-PBF IN725. The L-PBF IN725 in the heat-treated condition exhibits a strength-ductility-corrosion combination that meets the standard for its wrought counterpart.

Our efforts provide a starting point for using L-PBF to produce IN725 components for potential use in extreme environments.

Declaration of Competing Interest

The authors declare that they have no known competing financial interests or personal relationships that could have appeared to influence the work reported in this paper.

Data availability

The raw data required to reproduce these findings are available from the authors upon reasonable request.

Acknowledgements

This research was funded by the Ministry of Education of Singapore, Official Number: MOE2017-T2-2-119. We would like to acknowledge the Facility for Analysis, Characterisation, Testing and Simulation, Nanyang Technological University, Singapore, for use of their electron microscopy.

Appendix A. Supplementary data

Supplementary data to this article can be found online at https://doi.org/10.1016/j.matchar.2022.112454.

References

[1] T. DebRoy, T. Mukherjee, J.O. Milewski, J.W. Elmer, B. Ribic, J.J. Blecher, W. Zhang, Scientific, technological and economic issues in metal printing and their solutions, Nat. Mater. 18 (10) (2019) 1026–1032.
[2] T. DebRoy, T. Mukherjee, H.L. Wei, J.W. Elmer, J.O. Milewski, Metallurgy, mechanistic models and machine learning in metal printing, Nat. Rev. Mater. 6 (1) (2020) 48–68.
[3] D. Gu, X. Shi, R. Poprawe, D.L. Bourell, R. Setchi, J. Zhu, Material-structure-performance integrated laser-metal additive manufacturing, Science 372 (6545) (2021) eabg1487.
[4] A. Bandyopadhyay, K.D. Traxel, M. Lang, M. Juhasz, N. Eliaz, S. Bose, Alloy design via additive manufacturing: advantages, challenges, applications and perspectives, Mater. Today 52 (2022) 207–224.
[5] C. Panwisawas, Y.T. Tang, R.C. Reed, Metal 3D printing as a disruptive technology for superalloys, Nat. Commun. 11 (1) (2020) 2327.
[6] T. Watkins, H. Bilheux, K. An, A. Payzant, R. Dehoff, C. Duty, W. Peter, C. Blue, C. Brice, Neutron characterization, Adv. Mater. Process. 23 (2013).
[7] M.S. Pham, C. Liu, I. Todd, J. Lertthanasarn, Damage-tolerant architected materials inspired by crystal microstructure, Nature 565 (7739) (2019) 305–311.
[8] Y.M. Wang, T. Voisin, J.T. McKeown, J. Ye, N.P. Calta, Z. Li, Z. Zeng, Y. Zhang, W. Chen, T.T. Roehling, R.T. Ott, M.K. Santala, P.J. Depond, M.J. Matthews, A. V. Hamza, T. Zhu, Additively manufactured hierarchical stainless steels with high strength and ductility, Nat. Mater. 17 (1) (2018) 63–71.
[9] Q. Chao, V. Cruz, S. Thomas, N. Birbilis, P. Collins, A. Taylor, P.D. Hodgson, D. Fabijanic, On the enhanced corrosion resistance of a selective laser melted austenitic stainless steel, Scr. Mater. 141 (2017) 94–98.
[10] S.-W. Baek, E.J. Song, J.H. Kim, M. Jung, U.B. Baek, S.H. Nahm, Hydrogen embrittlement of 3-D printing manufactured austenitic stainless steel part for hydrogen service, Scr. Mater. 130 (2017) 87–90.
[11] S. Tekumalla, B. Selvarajou, S. Raman, S. Gao, M. Seita, The role of the solidification structure on orientation-dependent hardness in stainless steel 316L produced by laser powder bed fusion, Mater. Sci. Eng. A 833 (2022), 142493.
[12] A. Arabi-Hashemi, X. Maeder, R. Figi, C. Schreiner, S. Griffiths, C. Leinenbach, 3D magnetic patterning in additive manufacturing via site-specific in-situ alloy modification, Appl. Mater. Today 18 (2020), 100512.
[13] Y.C. Yeoh, G. Macchi, E. Jain, B. Gaskey, S. Raman, G. Tay, D. Verdi, A. Patran, A. M. Grande, M. Seita, Multiscale microstructural heterogeneity and mechanical property scatter in Inconel 718 produced by directed energy deposition, J. Alloys Compd. 887 (2021), 161426.
[14] K. Sofinowski, M. Wittwer, M. Seita, Encoding data into metal alloys using laser powder bed fusion, Addit. Manuf. 52 (2022), 102683.
[15] D.C. Hofmann, S. Roberts, R. Otis, J. Kolodziejska, R.P. Dillon, J.O. Suh, A. A. Shapiro, Z.K. Liu, J.P. Borgonia, Developing gradient metal alloys through radial deposition additive manufacturing, Sci. Rep. 4 (1) (2014) 5357.
[16] C.J. Todaro, M.A. Easton, D. Qiu, D. Zhang, M.J. Bermingham, E.W. Lui, M. Brandt, D.H. StJohn, M. Qian, Grain structure control during metal 3D printing by high-intensity ultrasound, Nat. Commun. 11 (1) (2020) 142.
[17] M. Seita, J.P. Hanson, S. Gradečak, M.J. Demkowicz, Probabilistic failure criteria for individual microstructural elements: an application to hydrogen-assisted crack initiation in alloy 725, J. Mater. Sci. 52 (5) (2017) 2763–2779.
[18] P. Kurnsteiner, M.B. Wilms, A. Weisheit, B. Gault, E.A. Jagle, D. Raabe, High-strength damascus steel by additive manufacturing, Nature 582 (7813) (2020) 515–519.
[19] L.E. Shoemaker, Alloys 625 and 725: trends in properties and applications, Superalloys 718 (625) (2005) 409–418.
[20] S.S. Shademan, J.W. Martin, A.P. Davis, Uns N07725 nickel alloy connection failure, Corrosion 2012 (2012).
[21] X. Zhao, J. Chen, X. Lin, W. Huang, Study on microstructure and mechanical properties of laser rapid forming Inconel 718, Mater. Sci. Eng. A 478 (1–2) (2008) 119–124.
[22] G.P. Dinda, A.K. Dasgupta, J. Mazumder, Laser aided direct metal deposition of Inconel 625 superalloy: microstructural evolution and thermal stability, Mater. Sci. Eng. A 509 (1–2) (2009) 98–104.
[23] L. Rickenbacher, T. Etter, S. Hövel, K. Wegener, High temperature material properties of IN738LC processed by selective laser melting (SLM) technology, Rapid Prototyp. J. 19 (4) (2013) 282–290.
[24] P. Kanagarajah, F. Brenne, T. Niendorf, H.J. Maier, Inconel 939 processed by selective laser melting: effect of microstructure and temperature on the mechanical properties under static and cyclic loading, Mater. Sci. Eng. A 588 (2013) 188–195.
[25] L.N. Carter, C. Martin, P.J. Withers, M.M. Attallah, The influence of the laser scan strategy on grain structure and cracking behaviour in SLM powder-bed fabricated nickel superalloy, J. Alloys Compd. 615 (2014) 338–347.
[26] G. Bi, C.-N. Sun, H.-C. Chen, F.L. Ng, C.C.K. Ma, Microstructure and tensile properties of superalloy IN100 fabricated by micro-laser aided additive manufacturing, Mater. Des. 60 (2014) 401–408.
[27] R. Acharya, R. Bansal, J.J. Gambone, S. Das, A coupled thermal, fluid flow, and solidification model for the processing of single-crystal alloy CMSX-4 through scanning laser epitaxy for turbine engine hot-section component repair (part I), Metall. Mater. Trans. B Process Metall. Mater. Process. Sci. 45 (6) (2014) 2247–2261.
[28] B. Du, L. Sheng, Z. Hu, C. Cui, J. Yang, X. Sun, Investigation on the microstructure and tensile behavior of a Ni-based IN792 superalloy, Adv. Mech. Eng. 10 (2) (2018), 1687814017752167.
[29] A. Ramakrishnan, G.P. Dinda, Microstructure and mechanical properties of direct laser metal deposited Haynes 282 superalloy, Mater. Sci. Eng. A 748 (2019) 347–356.
[30] R. Snell, S. Tammas-Williams, L. Chechik, A. Lyle, E. Hernández-Nava, C. Boig, G. Panoutsos, I. Todd, Methods for rapid pore classification in metal additive manufacturing, Jom 72 (1) (2019) 101–109.
[31] W. Cao, S.L. Chen, F. Zhang, K. Wu, Y. Yang, Y.A. Chang, R. Schmid-Fetzer, W. A. Oates, PANDAT software with PanEngine, PanOptimizer and PanPrecipitation for multi-component phase diagram calculation and materials property simulation, Calphad 33 (2) (2009) 328–342.
[32] Y.T. Tang, C. Panwisawas, J.N. Ghoussoub, Y. Gong, J.W.G. Clark, A.A.N. Németh, D.G. McCartney, R.C. Reed, Alloys-by-design: application to new superalloys for additive manufacturing, Acta Mater. 202 (2021) 417–436.
[33] C. Schwerz, F. Schulz, E. Natesan, L. Nyborg, Increasing productivity of laser powder bed fusion manufactured Hastelloy X through modification of process parameters, J. Manuf. Process. 78 (2022) 231–241.
[34] T. Mukherjee, T. DebRoy, Mitigation of lack of fusion defects in powder bed fusion additive manufacturing, J. Manuf. Process. 36 (2018) 442–449.
[35] R. Cunningham, C. Zhao, N. Parab, C. Kantzos, J. Pauza, K. Fezzaa, T. Sun, A. D. Rollett, Keyhole threshold and morphology in laser melting revealed by ultrahigh-speed x-ray imaging, Science 363 (6429) (2019) 849–852.
[36] ASTM B805–06(2017)e1, Standard Specification for Precipitation Hardening Nickel Alloys Bar and Wire, ASTM International, West Conshohocken, PA, 2017. www.astm.org.
[37] M.S. Wang, J.P. Hanson, S. Gradečak, M.J. Demkowicz, Cutting apart of γ'' precipitates by dislocations emitted from nanoscale surface notches in Ni-Base alloy 725, Mater. Res. Lett. 1 (2) (2013) 77–80.
[38] M. Seita, J.P. Hanson, S. Gradecak, M.J. Demkowicz, The dual role of coherent twin boundaries in hydrogen embrittlement, Nat. Commun. 6 (1) (2015) 6164.
[39] R.C. Reed, The Superalloys, Cambridge University Press, Cambridge, 2006.
[40] Y. Lei, K. Aoyagi, K. Aota, K. Kuwabara, A. Chiba, Critical factor triggering grain boundary cracking in non-weldable superalloy Alloy713ELC fabricated with selective electron beam melting, Acta Mater. 208 (2021), 116695.
[41] M. Prager, C. Shira, Welding of precipitation-hardening nickel- base alloys(welding precipitation hardenable Ni base alloys noting heat treatment, microfissuring, strain age cracking and other intricacies), Weld. Res. Counc. Bull. 128 (1968).
[42] D.G. Eskin, L. Katgerman, A quest for a new hot tearing criterion, Metall. Mater. Trans. A 38 (7) (2007) 1511–1519.
[43] M. Cloots, P.J. Uggowitzer, K. Wegener, Investigations on the microstructure and crack formation of IN738LC samples processed by selective laser melting using Gaussian and doughnut profiles, Mater. Des. 89 (2016) 770–784.
[44] X. Zhang, H. Chen, L. Xu, J. Xu, X. Ren, X. Chen, Cracking mechanism and susceptibility of laser melting deposited Inconel 738 superalloy, Mater. Des. 183 (2019), 108105.
[45] Y. Tian, D. McAllister, H. Colijn, M. Mills, D. Farson, M. Nordin, S. Babu, Rationalization of microstructure heterogeneity in INCONEL 718 builds made by the direct laser additive manufacturing process, Metall. Mater. Trans. A 45 (10) (2014) 4470–4483.
[46] L.L. Parimi, R.G. A, D. Clark, M.M. Attallah, Microstructural and texture development in direct laser fabricated IN718, Mater. Charact. 89 (2014) 102–111.
[47] S. Kou, A criterion for cracking during solidification, Acta Mater. 88 (2015) 366–374.
[48] J. Xu, Z. Wu, J. Niu, Y. Song, C. Liang, K. Yang, Y. Chen, Y. Liu, Effect of laser energy density on the microstructure and microhardness of Inconel 718 alloy fabricated by selective laser melting, Crystals 12 (9) (2022) 1243.
[49] M.J. Benoit, M. Mazur, M.A. Easton, M. Brandt, Effect of alloy composition and laser powder bed fusion parameters on the defect formation and mechanical properties of Inconel 625, Int. J. Adv. Manuf. Technol. 114 (3) (2021) 915–927.
[50] F. Geiger, K. Kunze, T. Etter, Tailoring the texture of IN738LC processed by selective laser melting (SLM) by specific scanning strategies, Mater. Sci. Eng. A 661 (2016) 240–246.

[51] S.-H. Sun, K. Hagihara, T. Nakano, Effect of scanning strategy on texture formation in Ni-25 at.%Mo alloys fabricated by selective laser melting, Mater. Des. 140 (2018) 307–316.
[52] G. Wang, H. Ouyang, C. Fan, Q. Guo, Z. Li, W. Yan, Z. Li, The origin of high-density dislocations in additively manufactured metals, Mater. Res. Lett. 8 (8) (2020) 283–290.
[53] S.W. Cheong, H. Weiland, Understanding a microstructure using GOS (grain orientation spread) and its application to recrystallization study of hot deformed Al-Cu-Mg alloys, in: Materials Science Forum, Trans Tech Publ, 2007, pp. 153–158.
[54] S. Gao, Z. Hu, M. Duchamp, P.S.S.R. Krishnan, S. Tekumalla, X. Song, M. Seita, Recrystallization-based grain boundary engineering of 316L stainless steel produced via selective laser melting, Acta Mater. 200 (2020) 366–377.
[55] D. Paulonis, J. Oblak, D. Duvall, Precipitation in nickel-base alloy 718, in: Pratt and Whitney Aircraft, Conn., Middletown, 1969.
[56] B. Dubiel, A. Kruk, E. Stepniowska, G. Cempura, D. Geiger, P. Formanek, J. Hernandez, P. Midgley, A. Czyrska-Filemonowicz, TEM, HRTEM, electron holography and electron tomography studies of γ' and γ'' nanoparticles in Inconel 718 superalloy, J. Microsc. 236 (2) (2009) 149–157.
[57] T.G. Gallmeyer, S. Moorthy, B.B. Kappes, M.J. Mills, B. Amin-Ahmadi, A. P. Stebner, Knowledge of process-structure-property relationships to engineer better heat treatments for laser powder bed fusion additive manufactured Inconel 718, Addit. Manuf. 31 (2020), 100977.
[58] H. Hack, R. Link, E. Knudsen, B. Baker, S. Olig, Mechanical properties of additive manufactured nickel alloy 625, Addit. Manuf. 14 (2017) 105–115.
[59] L. Huang, Y. Cao, J. Zhang, X. Gao, G. Li, Y. Wang, Effect of heat treatment on the microstructure evolution and mechanical behaviour of a selective laser melted Inconel 718 alloy, J. Alloys Compd. 865 (2021), 158613.
[60] S. Esmailzadeh, M. Aliofkhazraei, H. Sarlak, Interpretation of cyclic potentiodynamic polarization test results for study of corrosion behavior of metals: a review, Prot. Met. Phys. Chem. Surf. 54 (5) (2018) 976–989.
[61] B. Zhang, M. Xiu, Y.T. Tan, J. Wei, P. Wang, Pitting corrosion of SLM Inconel 718 sample under surface and heat treatments, Appl. Surf. Sci. 490 (2019) 556–567.
[62] K.N. Amato, S.M. Gaytan, L.E. Murr, E. Martinez, P.W. Shindo, J. Hernandez, S. Collins, F. Medina, Microstructures and mechanical behavior of Inconel 718 fabricated by selective laser melting, Acta Mater. 60 (5) (2012) 2229–2239.
[63] T. DebRoy, H.L. Wei, J.S. Zuback, T. Mukherjee, J.W. Elmer, J.O. Milewski, A. M. Beese, A. Wilson-Heid, A. De, W. Zhang, Additive manufacturing of metallic components – process, structure and properties, Prog. Mater. Sci. 92 (2018) 112–224.
[64] D. Zhang, A. Prasad, M.J. Bermingham, C.J. Todaro, M.J. Benoit, M.N. Patel, D. Qiu, D.H. StJohn, M. Qian, M.A. Easton, Grain refinement of alloys in fusion-based additive manufacturing processes, Metall. Mater. Trans. A 51 (9) (2020) 4341–4359.
[65] L.S. Aota, P. Bajaj, K.D. Zilnyk, E.A. Jägle, D. Ponge, H.R.Z. Sandim, D. Raabe, Recrystallization kinetics, mechanisms, and topology in alloys processed by laser powder-bed fusion: AISI 316L stainless steel as example, Materialia 20 (2021), 101236.
[66] ASTM ASTM B637-18, Standard Specification for Precipitation-Hardening and Cold Worked Nickel Alloy Bars, Forgings, and Forging Stock for Moderate or High Temperature Service, ASTM International, West Conshohocken, PA, 2018. www.astm.org.
[67] ASTM F3055-14a, Standard Specification for Additive Manufacturing Nickel Alloy (UNS N07718) with Powder Bed Fusion, ASTM International, West Conshohocken, PA, 2021. www.astm.org.
[68] E. Chlebus, K. Gruber, B. Kuźnicka, J. Kurzac, T. Kurzynowski, Effect of heat treatment on the microstructure and mechanical properties of Inconel 718 processed by selective laser melting, Mater. Sci. Eng. A 639 (2015) 647–655.
[69] W.M. Tucho, P. Cuvillier, A. Sjolyst-Kverneland, V. Hansen, Microstructure and hardness studies of Inconel 718 manufactured by selective laser melting before and after solution heat treatment, Mater. Sci. Eng. A 689 (2017) 220–232.
[70] W.M. Tucho, V. Hansen, Characterization of SLM-fabricated Inconel 718 after solid solution and precipitation hardening heat treatments, J. Mater. Sci. 54 (1) (2018) 823–839.
[71] G. Marchese, M. Lorusso, S. Parizia, E. Bassini, J.-W. Lee, F. Calignano, D. Manfredi, M. Terner, H.-U. Hong, D. Ugues, M. Lombardi, S. Biamino, Influence of heat treatments on microstructure evolution and mechanical properties of Inconel 625 processed by laser powder bed fusion, Mater. Sci. Eng. A 729 (2018) 64–75.
[72] Heat Treatment, Wrought Nickel Alloy and Cobalt Alloy Parts, AMS 2774, SAE international, Warrendale, PA, 2020.
[73] C.Y. Jo, H.Y. Cho, H.M. Kim, Effect of recrystallisation on microstructural evolution and mechanical properties of single crystal nickel base superalloy CMSX-2 part 1nnn- microstructural evolution during recrystallisation of single crystal, Mater. Sci. Technol. 19 (12) (2003) 1665–1670.
[74] M. Ni, C. Chen, X. Wang, P. Wang, R. Li, X. Zhang, K. Zhou, Anisotropic tensile behavior of in situ precipitation strengthened Inconel 718 fabricated by additive manufacturing, Mater. Sci. Eng. A 701 (2017) 344–351.
[75] N. Kouraytem, J. Varga, B. Amin-Ahmadi, H. Mirmohammad, R.A. Chanut, A. D. Spear, O.T. Kingstedt, A recrystallization heat-treatment to reduce deformation anisotropy of additively manufactured Inconel 718, Mater. Des. 198 (2021), 109228.
[76] J. Schröder, T. Mishurova, T. Fritsch, I. Serrano-Munoz, A. Evans, M. Sprengel, M. Klaus, C. Genzel, J. Schneider, G. Bruno, On the influence of heat treatment on microstructure and mechanical behavior of laser powder bed fused Inconel 718, Mater. Sci. Eng. A 805 (2021), 140555.
[77] A. Kreitcberg, V. Brailovski, S. Turenne, Effect of heat treatment and hot isostatic pressing on the microstructure and mechanical properties of Inconel 625 alloy processed by laser powder bed fusion, Mater. Sci. Eng. A 689 (2017) 1–10.
[78] G. Marchese, S. Parizia, M. Rashidi, A. Saboori, D. Manfredi, D. Ugues, M. Lombardi, E. Hryha, S. Biamino, The role of texturing and microstructure evolution on the tensile behavior of heat-treated Inconel 625 produced via laser powder bed fusion, Mater. Sci. Eng. A 769 (2020), 138500.
[79] S. Luo, W. Huang, H. Yang, J. Yang, Z. Wang, X. Zeng, Microstructural evolution and corrosion behaviors of Inconel 718 alloy produced by selective laser melting following different heat treatments, Addit. Manuf. 30 (2019), 100875.
[80] A. Shahriari, L. Khaksar, A. Nasiri, A. Hadadzadeh, B.S. Amirkhiz, M. Mohammadi, Microstructure and corrosion behavior of a novel additively manufactured maraging stainless steel, Electrochim. Acta 339 (2020), 135925.